

Global particle in cell simulation of fusion plasma in cylindrical coordinates

A. Kuley,^{1,2, a)} J. Bao,² Z. Lin,² and G. Y. Sun¹

¹⁾College of Physical Science and Technology, Xiamen University, Xiamen 361005, China

²⁾Department of Physics and Astronomy, University of California Irvine, CA 92697, USA

(Dated: 15 February 2017)

We report the recent upgrade of gyrokinetic toroidal code (GTC), which enables global simulations coupling the core and scrape-off layer (SOL) across the separatrix by using cylindrical coordinates with field-aligned particle-grid interpolation. With the interfacing with EFIT equilibrium and LamyRidge equilibrium, GTC code can be applied for the global geometry simulation for both tokamak and field reversed configuration (FRC). The fully kinetic particle trajectory integrator is also implemented in cylindrical coordinates by using Boris push method with conserving energy and canonical angular momentum.

I. INTRODUCTION

One of the important challenges for the viable operating regime for ITER and future fusion reactors is associated with the nonlinear turbulent dynamics of plasma in the scrape-off layer (SOL).¹ The plasma characteristics in SOL will govern the overall confinement properties of the device. Plasma properties at the SOL also regulate the heat load to the tokamak wall (plasma wall interaction), level of fusion ash, impurity dynamics, sheath physics and plasma shaping effects. Moreover, the SOL dynamics also determines the current drive performance due to density threshold (parametric decay instabilities) of radio frequency waves.² Study of SOL plasma dynamics is challenging due to multiple temporal and spatial and temporal scales associated with different energy sources (instabilities). Fluid simulation transport codes such as UEDGE,³ SOLPS⁴ are normally used to simulate the SOL dynamics. These fluid codes are based on the set of fluid transport equations that are equivalent to the set of Braginskii equations.⁵ However, the results show a number of discrepancies between experiments and fluid simulation including radial electric field, parallel ion flow, impurity radiation, etc in the SOL.⁶⁻⁸ It is believed that the kinetic effect will play a crucial role in the SOL such as ion orbit loss,⁹ X point loss,¹⁰ non-local turbulent transport,¹¹ plasma sheath,¹² parametric decay instabilities,^{2,13-15} etc. To correctly model many of these effects requires kinetic approach, which covers the closed, and open field line regions across the separatrix, and includes realistic SOL physics and tokamak geometry. Also due to the difficulty of accessibility of diagnostics, simulation at SOL can provide the predictive capability of plasma dynamics for present and future reactors such as ITER and DEMO. After rigorous development, massively parallel kinetic simulation based on first-principles has emerged as an efficient method for describing the complex physics of turbulent transport.

GTC is involved in the study of plasma trans-

port in the core region for last two decades.¹⁶ GTC is a well-benchmarked, first principles code which has been extensively applied to study neoclassical transport,^{17,18} microturbulence,¹⁹⁻²⁴ mesoscale Alfvén eigenmodes²⁵⁻²⁸ excited by energetic particles, macroscopic MHD modes²⁹⁻³¹ (kink and tearing modes) and radio frequency (RF) waves³²⁻³⁸ in the core region.

GTC normally use conventional magnetic flux coordinates, in which the equations of motion encounter a mathematical singularity of metric on the magnetic separatrix surface. Since the field lines in the SOL region are not closed, the periodic magnetic scalar potential becomes meaningless. Recently, GTC has been extended to study instabilities in the SOL region of the field reverse configuration (FRC) using Boozer coordinates.^{21,39,40} For FRC geometry the equilibrium is approximately symmetric over $Z=0$ axis, helps to enforce periodicity across the Z boundary, during Fourier decomposition on each flux surface, where Z represents the horizontal direction in FRC. One of the consequences of enforcing periodicity is that the spacing of Boozer coordinate poloidal angle depends on the length of the simulation domain. A wider domain in simulation domain produces large spacing between constant Boozer coordinate poloidal angle surfaces. As a result the Boozer coordinate poloidal angle becomes discontinuous across the separatrix. That's why the electrostatic simulations are carried out either in the core or SOL region separately with no cross-separatrix coupling.

The present goal of GTC is to develop a new nonlinear particle simulation model to couple the core and SOL region, which involve the treatment of the separatrix by reading the equilibrium data files generated from the experimental equilibrium reconstruction such as EFIT^{41,42} (for tokamak) and LamyRidge⁴³ (for FRC). A particular feature in the upgraded GTC is the use of cylindrical coordinate system for the advancement of the particle dynamics, which allows particle motion in arbitrary shaped flux surfaces including the magnetic separatrix and the magnetic X-point.

As a first step in developing this nonlinear particle simulation model, the particle dynamics of guiding center (GC) pusher associated with the low frequency waves ($\omega \ll \omega_{ci}$) for FRC and tokamak are presented in this

^{a)}Electronic mail: akuley@uci.edu

paper, where ω_{ci} is the ion cyclotron frequency. We also developed the fully kinetic (FK) particle pusher to capture the high frequency ($\omega > \omega_{ci}$) modes and large orbit physics. Finally we construct the field aligned mesh to take advantage of the smallest number of grid points in the direction of the magnetic field with high resolution in any given poloidal plane using more fundamental cylindrical coordinates rather than the flux coordinates. Field aligned coordinate approaches have been used in coupled of turbulence simulation code such as GTC,²⁴ XGC1,⁴⁴ FENICA,⁴⁵ GEM,⁵⁰ etc. The gain in computational efficiency by using the suitable coordinates and computational mesh will help to optimize the turbulence simulation of large device like ITER.

The paper is organized as follows:

II. REPRESENTATION OF EQUILIBRIUM AND COORDINATE SYSTEM

In plasma, the physical quantities are classified into equilibrium and fluctuating part. The equilibrium is described by the Grad-Shafranov equation, while the fluctuation is described by the instability, which leads to plasma transport. The equilibrium magnetic field configuration used in the upgraded GTC version are from EFIT and LamyRidge. The equilibrium in tokamaks and FRC can be described by magnetic flux coordinates to take the advantage of divergence free magnetic field. Secondly, the plasma profile such as plasma temperature, density depends on the flux only. In recent GTC version we use cylindrical toroidal coordinates (R, ζ, Z) to represent the electromagnetic fields, where R is the radial position in horizontal direction, ζ is the toroidal angle and Z is the direction of the torus symmetry axis [cf. Fig1]. The representation of the magnetic field for an axisymmetric system is

$$\vec{B} = \nabla\psi(R, Z) \times \nabla\zeta + \frac{F(\psi)}{R} \hat{\zeta}, \quad (1)$$

where $\psi(R, Z)$ is the poloidal flux function, labels the magnetic surfaces for both close and open field lines and $F(\psi)$ is the poloidal current function, which provide the components of magnetic field in cylindrical coordinates (R, ζ, Z) as:

$$B_R = -\frac{1}{R} \frac{\partial\psi}{\partial Z}, \quad B_Z = \frac{1}{R} \frac{\partial\psi}{\partial R}, \quad B_\zeta = \frac{F(\psi)}{R}, \quad (2)$$

and the Jacobian of this system can be written as

$$J^{-1} = \nabla R \cdot (\nabla\zeta \times \nabla Z). \quad (3)$$

The cylindrical toroidal coordinate system relates to the standard Cartesian system as follows

$$\begin{aligned} x &= R \cos \zeta, \\ y &= R \sin \zeta, \\ z &= Z. \end{aligned} \quad (4)$$

By defining contravariant basis $\vec{e}^R = \nabla R$, $\vec{e}^\zeta = \nabla\zeta$, $\vec{e}^Z = \nabla Z$ the velocity and the electric field can be written as

$$\vec{v} = v^R \vec{e}_R + v^\zeta \vec{e}_\zeta + v^Z \vec{e}_Z, \quad (5)$$

$$\vec{E} = -\nabla\phi = -\left[\frac{\partial\phi}{\partial R} \nabla R + \frac{\partial\phi}{\partial \zeta} \nabla \zeta + \frac{\partial\phi}{\partial Z} \nabla Z \right], \quad (6)$$

where

$$\begin{aligned} v^R &= \dot{R}, \quad v^\zeta = \dot{\zeta}, \quad v^Z = \dot{Z}, \\ \vec{e}_R &= \cos \zeta \hat{x} + \sin \zeta \hat{y}, \\ \vec{e}_\zeta &= -R \sin \zeta \hat{x} + R \cos \zeta \hat{y}, \\ \vec{e}_Z &= \hat{z}. \end{aligned} \quad (7)$$

The GTC code inputs from EFIT and LamyRidge only provide equilibrium on a coarse mesh, which usually contains a few tens of grid points in the R and Z directions. However, the micro-scale turbulence demands much denser grid points in R and Z directions. Therefore, it is necessary to map the equilibrium mesh to dense computational mesh to achieve sufficient numerical accuracy. Generally two classes of functions are used to interpolate the magnetic geometry and plasma profiles, one dimensional function $f(\psi)$ or two dimensional function $f(R, Z)$. For 1D function $f(\psi)$, such as poloidal current function $F(\psi)$, we can use the following B-spline representation²⁴

$$f(\psi) = f(1, i) + f(2, i) \Delta\psi + f(3, i) \Delta\psi^2, \quad (8)$$

where $\Delta\psi = \psi_{i+1} - \psi_i$, $i = 0, 1, 2, \dots, n\psi$. The 2D function $f(R, Z) = \sum_n \mathbb{F}_n(R) \mathbb{G}_n(Z)$ can be expressed as

$$\begin{aligned} f(R, Z) &= f(1, i, j) + f(2, i, j) \Delta R + f(3, i, j) \Delta R^2 + \\ &+ f(4, i, j) \Delta Z + f(5, i, j) \Delta R \Delta Z + f(6, i, j) \Delta Z \Delta R^2 + \\ &+ f(7, i, j) \Delta Z^2 + f(8, i, j) \Delta R \Delta Z^2 + f(9, i, j) \Delta R^2 \Delta Z^2, \end{aligned} \quad (9)$$

where $\Delta R = R_{i+1} - R_i$, $i = 0, 1, 2, \dots, nR$, and $\Delta Z = Z_{j+1} - Z_j$, $j = 0, 1, 2, \dots, nZ$. Eq.(9) is derived by using the 1D B-spline function of $\mathbb{F}_n(R)$ and $\mathbb{G}_n(Z)$ [cf. Eq.(8)]. Fig.2(a) and Fig.2(b) represent the equilibrium poloidal current function on uniform flux grid and poloidal flux function on rectangular R-Z grid for DIII-D shot #158103 at 3050 ms, respectively. In GTC we use these two functions in Eq.(2) to calculate the magnetic field components [cf. Fig.3]. In particle pusher we interpolate these field quantities at the particle position using 2D spline function, as described in Eq.(9).

III. PHYSICS MODEL FOR PARTICLE DYNAMICS

The efficiency of particle simulation strongly depends on advancement of dynamical quantities. In GTC we

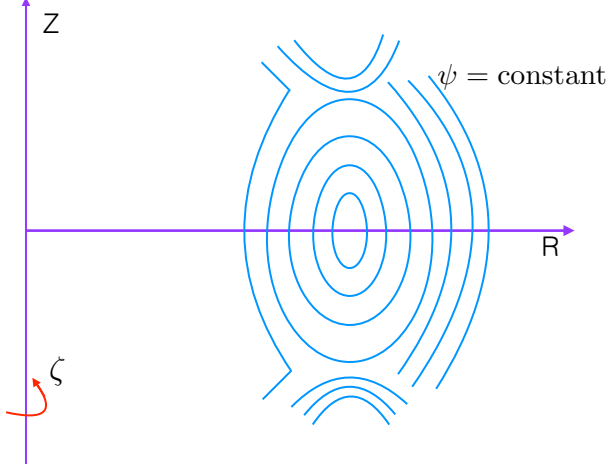


FIG. 1. Schematic diagram of the cylindrical coordinates (R, ζ, Z) for a cylindrical toroidal system.

have developed the particle pusher for fully kinetic particles and guiding center particles using cylindrical coordinate (R, ζ, Z) . The physics model for the fully kinetic dynamics, guiding center dynamics and the numerical methods associated with the time advancement of the physical quantities (particle position and guiding center) are described in the following sections.

A. Fully kinetic dynamics

Particle dynamics is described by the six dimensional Vlasov equation,

$$\left[\frac{\partial}{\partial t} + \vec{v} \cdot \nabla + \frac{q_c}{m} (\vec{\mathbb{E}} + \vec{v} \times \vec{B}) \cdot \frac{\partial}{\partial \vec{v}} \right] f_{FK} = 0, \quad (10)$$

where f_{FK} is the fully kinetic distribution function, q_c is the particle charge, and m is the particle mass.

The evolution of the particle distribution function f_{FK} can be described by the Newtonian equation of motion in the presence of self-consistent electromagnetic field as follows:

$$\frac{d}{dt} \vec{r} = \vec{v}, \quad \frac{d}{dt} \vec{v} = \frac{q_c}{m} [\vec{\mathbb{E}} + \vec{v} \times \vec{B}]. \quad (11)$$

In our simulation we compute the marker particle trajectory [Eq.(11)] by the time centered Boris push method^{32,34,46-48} as discussed in section B. The Lagrangian for the single particle motion in the cylindrical coordinates is written as

$$\mathcal{L} = \frac{m}{2} [\dot{R}^2 + R^2 \dot{\zeta}^2 + \dot{Z}^2] + q_c [\dot{R} A_R + R \dot{\zeta} A_\zeta + \dot{Z} A_Z] - q_c \phi, \quad (12)$$

where \vec{A} is the vector potential. Now the components of generalized momenta are

$$\begin{aligned} p_R &= \frac{\partial \mathcal{L}}{\partial \dot{R}} = m \dot{R} + q_c A_R, \\ p_\zeta &= \frac{\partial \mathcal{L}}{\partial \dot{\zeta}} = m R^2 \dot{\zeta} + q_c R A_\zeta, \\ p_Z &= \frac{\partial \mathcal{L}}{\partial \dot{Z}} = m \dot{Z} + q_c A_Z. \end{aligned} \quad (13)$$

In our simulation we use the poloidal flux function ψ , rather than the vector potential \vec{A} to represent the magnetic field components. Two constants of motion for fully kinetic dynamics in cylindrical coordinates are defined by:⁵⁰

- Kinetic Energy

$$E = (m/2)[(v^R)^2 + (Rv^\zeta)^2 + (v^Z)^2],$$

- Toroidal angular momentum

$$p_\zeta = m R^2 v^\zeta + q_c \psi.$$

B. Boris push for fully kinetic particle dynamics

Boris scheme is the most widely used orbit integrator in explicit particle-in-cell (PIC) simulation of plasmas. In this paper we have extended our Boris push scheme from Boozer coordinates³⁴ to cylindrical coordinates. This scheme offers second order accuracy while requiring only one force (or field) evaluation per step. The interplay between the PIC cycle and the Boris scheme is schematically represented in Fig.6. At the beginning of each cycle the position of the particles and their time centered velocity $\vec{v}(t - 1/2)$, weight $w(t)$, as well as the grid based electromagnetic fields $\vec{\mathbb{E}}(t)$, $\vec{B}(t)$ are given.

In the first step, we add the first half of the electric field acceleration to the velocity $\vec{v}(t - 1/2)$ to obtain the velocity at the particle position at t as follows:

$$\vec{u}(t) = \vec{v}(t - 1/2) + \frac{q_c}{m} \frac{\Delta t}{2} \vec{\mathbb{E}}(t) \quad (14)$$

One may write the components of velocity at particle position at t as

$$\begin{aligned} u^\alpha(t) &= \sum_{\beta=R,\zeta,Z} v^\beta(t - 1/2) \vec{e}_\beta(t - 1/2) \cdot \nabla \alpha(t) \\ &\quad + \frac{q_c}{m} \frac{\Delta t}{2} \vec{\mathbb{E}}(t) \cdot \nabla \alpha(t), \end{aligned} \quad (15)$$

where $\alpha = R, \zeta, Z$. For an orthogonal cylindrical system

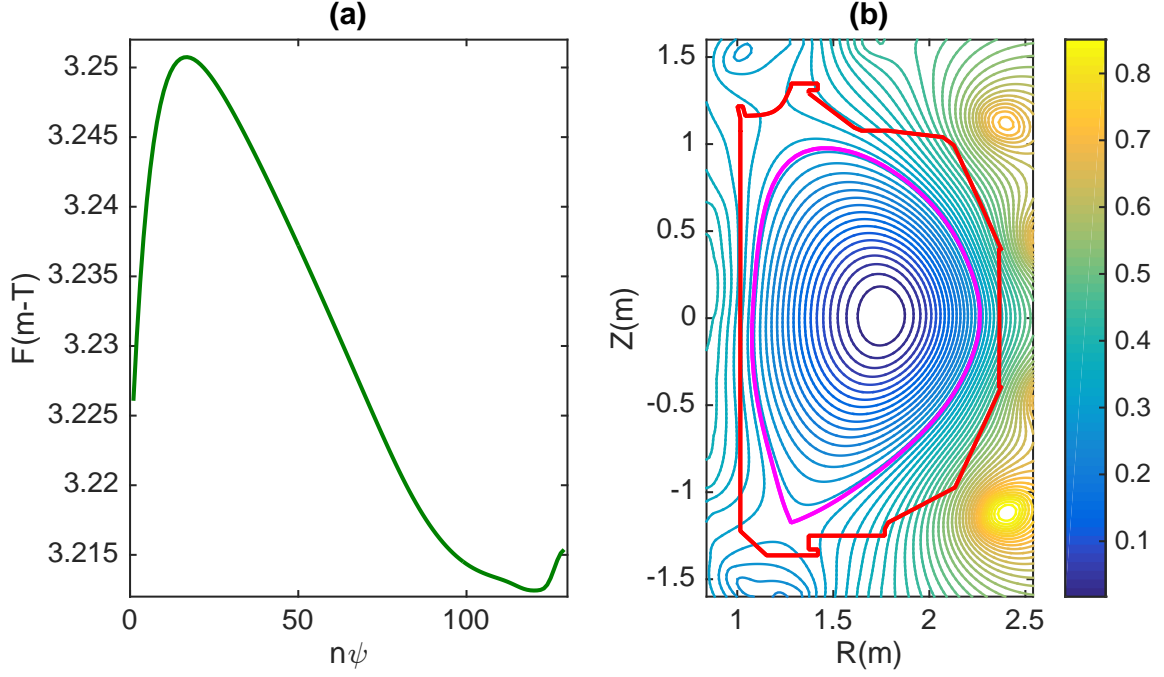


FIG. 2. (a) Poloidal current function $F(\psi)$ in m-T on uniform flux grid, and (b) poloidal flux function in web/rad on rectangular (R, Z) grid points for DIII-D shot #158103 at 3050 ms. The magnitude of the flux function is indicated by color. Last close surface and limiter points are represented by magenta and red line, respectively.

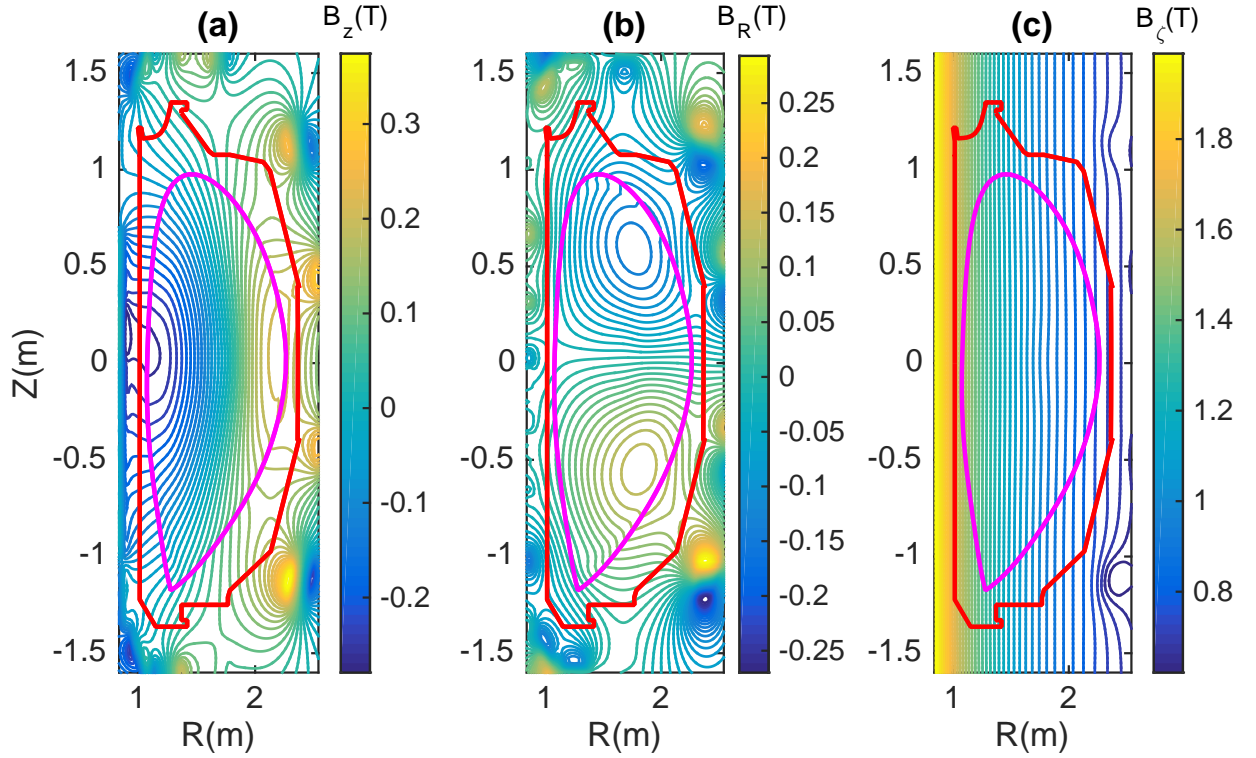


FIG. 3. Components of magnetic field (a) B_z , (b) B_R and (c) B_ϕ for DIII-D shot #158103 at 3050 ms. The magnitude of the magnetic field components are indicated by color. Last close surface and limiter points are represented by magenta and red line, respectively.

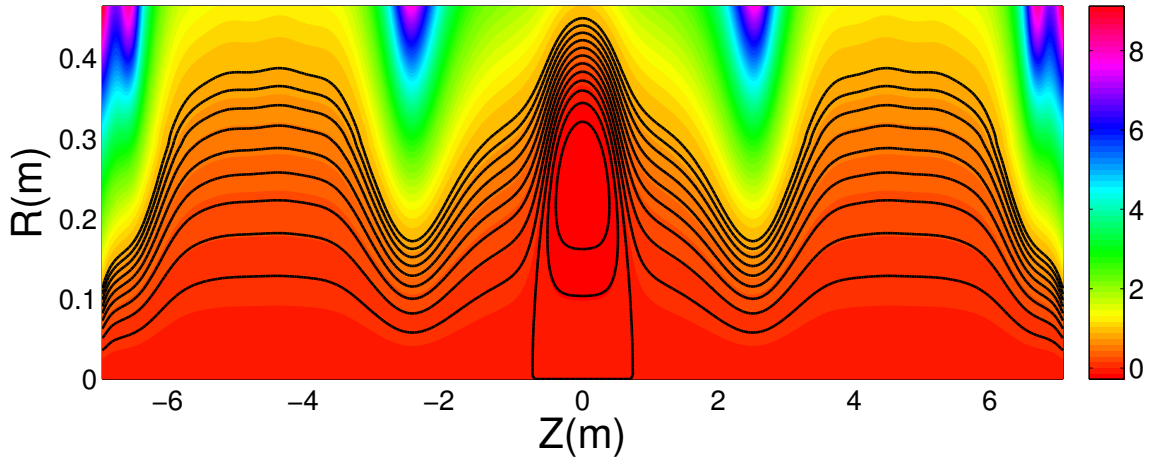


FIG. 4. Poloidal flux function on rectangular (R, Z) grid points for FRC geometry.

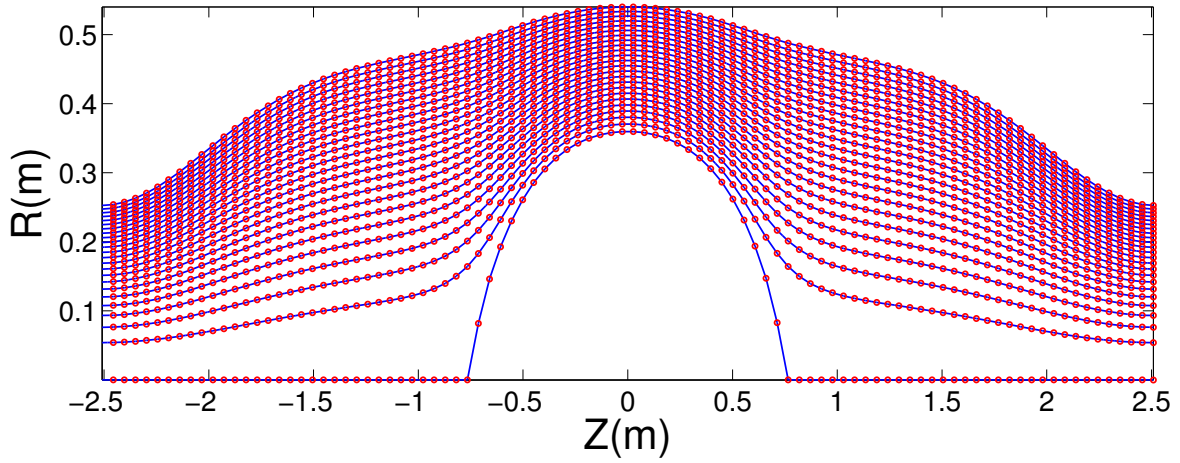


FIG. 5. GTC computational grids for SOL region of FRC.

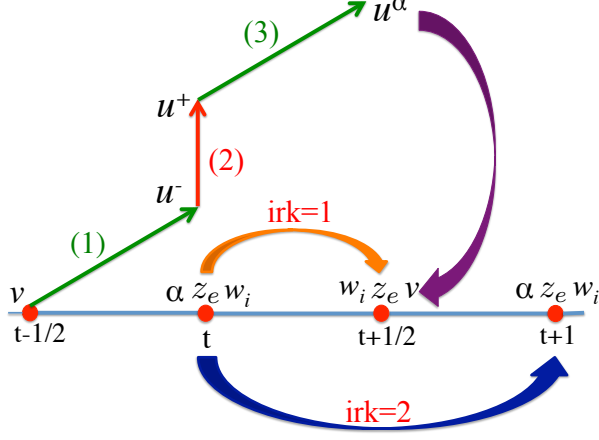


FIG. 6. Schematic diagram for the PIC cycle, Boris push and second order Runge Kutta method. The first step indicates the addition of the first half of the electric field acceleration to the velocity ($v \rightarrow u^-$). The second step is rotation of the velocity vector ($u^- \rightarrow u^+$). In the third step, we add the second half of the electric field impulse to the rotated velocity component ($u^+ \rightarrow u^\alpha, \alpha = R, \zeta, Z$). Guiding center is updated using the second order Runge-Kutta (irk=1 and irk=2) method. Dark purple blue indicates the transformation from $u^\alpha \rightarrow v$, which is needed to update the fully kinetic particle position [cf. Eq.(20)]. Reprinted with permission from A. Kuley et al., Phys. Plasmas 22, 102515 (2015). Copyright 2015 AIP Publishing LLC.

the above Eq. (15) can be rewritten as as follows:

$$\begin{aligned}
 u^{R-}(t) &= A_1 v^R(t-1/2) + B_1 R(1) v^\zeta(t-1/2) \\
 &\quad + \frac{q_c}{m} \frac{\Delta t}{2} \vec{E}(t) \cdot \nabla R(t), \\
 u^{\zeta-}(t) &= R(2) \left[\frac{A_1 R(1)}{g_{\zeta\zeta}(t)} v^\zeta(t-1/2) - \frac{B_1}{g_{\zeta\zeta}(t)} v^R(t-1/2) \right] \\
 &\quad + \frac{q_c}{m} \frac{\Delta t}{2} \vec{E}(t) \cdot \nabla \zeta(t), \\
 u^{Z-}(t) &= v^Z(t-1/2) + \frac{q_c}{m} \frac{\Delta t}{2} \vec{E}(t) \cdot \nabla Z(t), \quad (16)
 \end{aligned}$$

where $A_1 = \cos(\zeta_2 - \zeta_1)$, $B_1 = \cos \zeta_1 \sin \zeta_2 - \sin \zeta_1 \cos \zeta_2$, $\zeta_1 = \zeta(t-1/2)$, $\zeta_2 = \zeta(t)$, $R(1) = R(t-1/2)$ and $R(2) = R(t)$.

In the second step we consider the rotation of the velocity at time (t) . Rotated vector can be written as

$$\vec{u}^+(t) = \vec{u}^-(t) + \vec{u}^-(t) \times \vec{s}(t) + [\vec{u}^-(t) \times \vec{T}(t)] \times \vec{s}(t), \quad (17)$$

where $\vec{T} = (q_c \vec{B}/m)(\Delta t/2)$ and $\vec{s} = 2\vec{T}/(1 + T^2)$. The components of rotated vector become

$$\begin{aligned}
 u^{R+}(t) &= \left[1 - PQ \left(B_Z^2 + B_\zeta^2 \right) \right] u^{R-}(t) \\
 &\quad + \left[PQ B_R B_\zeta R + P B_Z \frac{g_{\zeta\zeta}}{J} \right] u^{\zeta-}(t) \\
 &\quad + \left[PQ B_R B_Z - P B_\zeta R \frac{1}{J} \right] u^{Z-}(t), \quad (18)
 \end{aligned}$$

$$\begin{aligned}
 u^{\zeta+}(t) &= \left[1 - PQ \left(B_R^2 + B_Z^2 \right) \right] u^{\zeta-}(t) \\
 &\quad + \left[PQ B_R B_\zeta R g^{\zeta\zeta} - P B_Z \frac{1}{J} \right] u^{R-}(t) \\
 &\quad + \left[PQ B_Z B_\zeta R g^{\zeta\zeta} + P B_R \frac{1}{J} \right] u^{Z-}(t), \quad (19)
 \end{aligned}$$

$$\begin{aligned}
 u^{Z+}(t) &= \left[1 - PQ \left(B_R^2 + B_\zeta^2 \right) \right] u^{Z-}(t) \\
 &\quad + \left[PQ B_Z B_\zeta R - P B_R \frac{g_{\zeta\zeta}}{J} \right] u^{\zeta-}(t) \\
 &\quad + \left[PQ B_R B_Z + P R B_\zeta \frac{1}{J} \right] u^{R-}(t), \quad (20)
 \end{aligned}$$

where $Q = (q_c/m)(\Delta t/2)$, $P = 2/(1 + T^2)(q_c/m)(\Delta t/2)$, $g_{\zeta\zeta} = R^2$, and $J^2 = \det(g_{\alpha\beta}) = R^2$. In the third step, we add the other half electric acceleration to the rotated vectors to obtain the velocity at time $(t + 1/2)$

$$u^\alpha(t + 1/2) = u^{\alpha+}(t) + \frac{q_c}{m} \frac{\Delta t}{2} \vec{E}(t) \cdot \nabla \alpha(t). \quad (21)$$

To update the particle position we need to recover $\vec{v}(t+1/2)$, which can be done through the following transformation (cf. Fig.6 dark purple arrow)

$$v^\gamma(t+1/2) = \sum_{\alpha=R,\zeta,Z} u^\alpha(t+1/2) \vec{e}_\alpha(t) \cdot \nabla \gamma(t+1/2), \quad (22)$$

where $\gamma = R, \zeta, Z$. However, the basis vector $\nabla \gamma(t + 1/2)$ is still unknown, since $\gamma(t + 1/2)$ does not exist in standard leap-frog scheme. Here we use an estimator for $\gamma(t + 1/2)$ as

$$\gamma(t + 1/2) = \gamma(t) + u^\gamma(t + 1/2) \frac{\Delta t}{2}. \quad (23)$$

After we find the velocity at time $(t+1/2)$, we can update the particle position using the leap-frog scheme as

$$\gamma(t + 1) = \gamma(t) + v^\gamma(t + 1/2) \Delta t. \quad (24)$$

In Eq.(22) we have the dot-product of two basis vectors at different time steps. We have evaluated this equation in the similar fashion as described in Eqs. (15)-(16).

In this section we have discussed the time advancement of the dynamical quantities like velocity and position of the particle in the time centered manner. However, for the self-consistent simulation we need to update particle weight, guiding center and electric field. We will use the second order Runge-Kutta (RK) method, to advance these quantities.^{34,35}

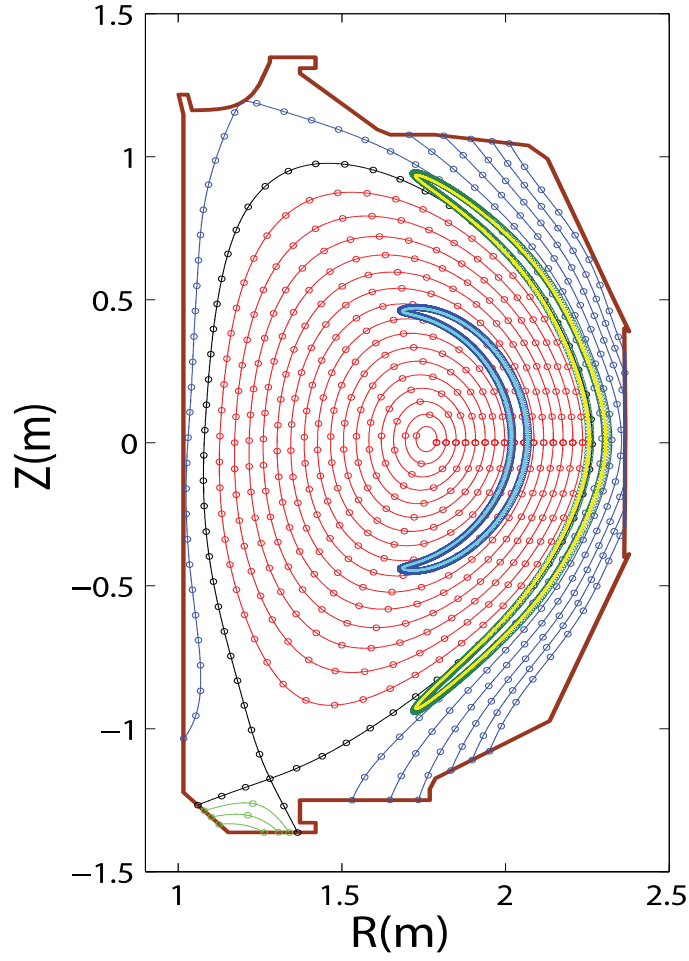


FIG. 7. GTC computational grids on a poloidal plane coupling core and SOL, and fully kinetic (blue and green) and guiding center (cyan and yellow) calculations of trapped particle orbits in the core (51.66keV) and cross separatrix (59.42keV) for DIII-D shot #158103 at 3050 ms. Field aligned mesh at the core, separatrix, SOL and private regions are represented by red, black, blue, and green, respectively. Last close surface and limiter points are represented by black and dark brown line, respectively.

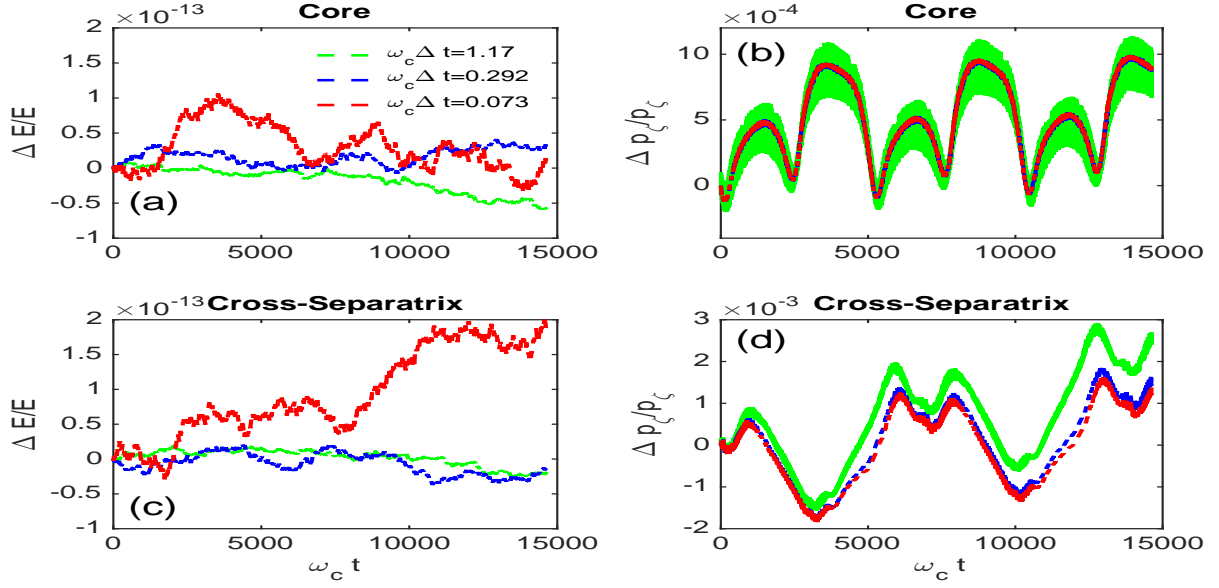


FIG. 8. Time step convergence of fully kinetic Boris integrator. Fig.(a), Fig.(c) represent the relative energy error and Fig.(b), Fig.(d) show relative canonical angular momentum error for DIII-D geometry core and cross-separatrix region, respectively.

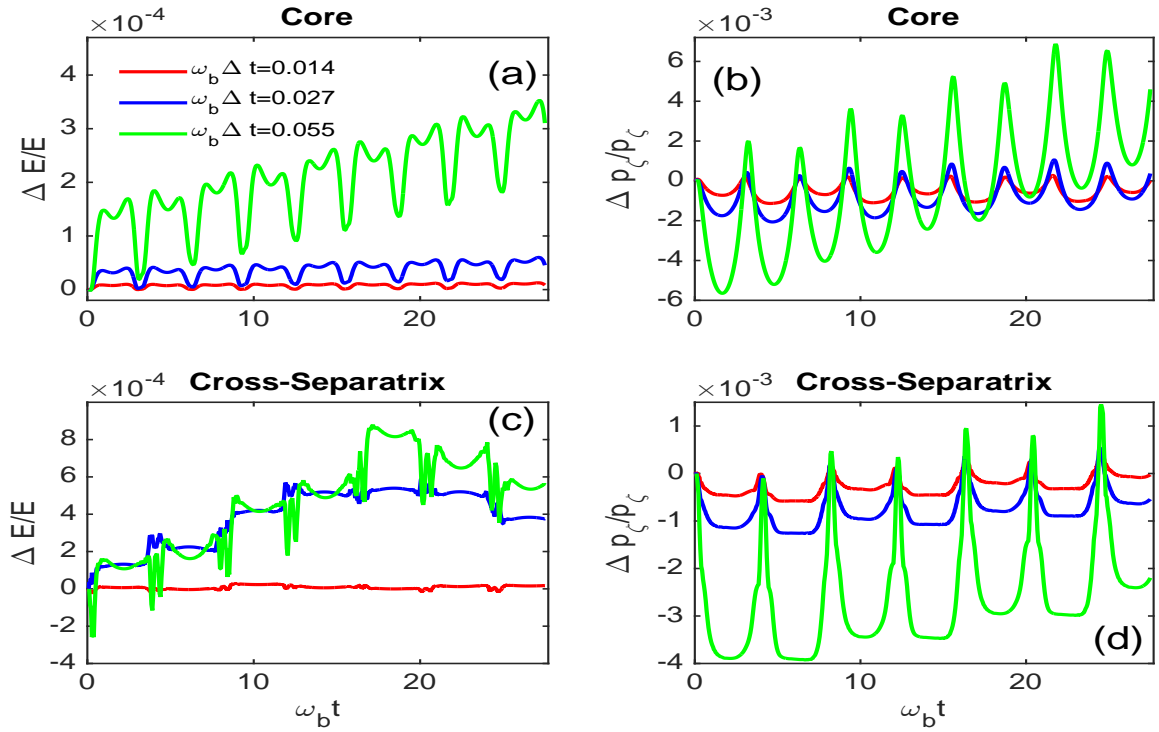


FIG. 9. Time step convergence of guiding center second order Runge Kutta integrator. Fig.(a), Fig.(c) represent the relative energy error and Fig.(b), Fig.(d) show relative canonical angular momentum error for DIII-D geometry core and cross-separatrix region, respectively.

TABLE I. Initial condition for FK integrator (DIII-D)

Parameter	Core	Cross-Separatrix
R/R_0	1.154	1.289
Z/R_0	0.0	0.0
ζ	1.570	1.570
$v^R/\omega_c R_0$	3.371×10^{-3}	3.371×10^{-3}
$v^Z/\omega_c R_0$	5.371×10^{-3}	5.371×10^{-3}
v^ζ/ω_c	1.271×10^{-3}	1.271×10^{-3}

TABLE II. Initial condition for GC integrator (DIII-D)

Parameter	Core	Cross-Separatrix
R/R_0	1.147	1.281
Z/R_0	0.0	0.0
ζ	1.570	1.570
$v_\parallel/\omega_c R_0$	2.547×10^{-3}	3.017×10^{-3}
$\sqrt{\mu B_0}/\omega_c R_0$	4.545×10^{-3}	4.642×10^{-3}

C. Guiding center dynamics

Particle dynamics is described by the five-dimensional phase space

$$\left[\frac{\partial}{\partial t} + \vec{X} \cdot \nabla + v_\parallel \frac{\partial}{\partial v_\parallel} \right] f_{GC} = 0, \quad (25)$$

where f_{GC} is the guiding center distribution function, \vec{X} is the guiding center position and v_\parallel is the parallel velocity. The evolution of the guiding center distribution function can be described by the following equations of guiding center motion:⁴⁹

$$\begin{aligned} \dot{\vec{X}} &= v_\parallel \hat{b} + \vec{v}_E + \vec{v}_c + \vec{v}_g, \\ \dot{v}_\parallel &= -\frac{1}{m} \frac{\vec{B}^*}{B} \cdot (\mu \nabla B + q_c \nabla \phi), \end{aligned} \quad (26)$$

where $\vec{B}^* = \vec{B} + B v_\parallel / \omega_c \nabla \times \hat{b}$, and $\mu = m v_\perp^2 / 2B$. The $\vec{E} \times \vec{B}$ drift velocity \vec{v}_E , the grad-B drift velocity \vec{v}_g and curvature drift velocity \vec{v}_c are given by

$$\begin{aligned} \vec{v}_E &= \frac{c \hat{b} \times \nabla \phi}{B}, \\ \vec{v}_g &= \frac{\mu}{m \omega_c} \hat{b} \times \nabla B, \\ \vec{v}_c &= \frac{v_\parallel^2}{\omega_c} \nabla \times \hat{b}. \end{aligned} \quad (27)$$

In GC description following order is adopted:

$$\frac{\omega}{\omega_c} \sim \frac{k_\parallel}{k_\perp} \sim \frac{q_c \phi}{T_c} \sim \mathcal{O}(\epsilon)$$

Two constants of motion for guiding center dynamics are defined by:

- Kinetic Energy

$$E = (m/2) v_\parallel^2 + \mu B,$$

- Toroidal angular momentum

$$p_\zeta = m v_\parallel (B_\zeta / B) + q_c \psi.$$

For an axisymmetric system, Eq. (26) can be rewritten in cylindrical coordinate (R, ζ, Z) as

$$v^R = v_\parallel \frac{B_R}{B} + \frac{c}{B} \frac{B_\zeta}{B} \frac{\partial \phi}{\partial Z} - \frac{v_\parallel^2}{\omega_c} \frac{\partial}{\partial Z} \left(\frac{B_\zeta}{B} \right) + \frac{\mu}{m \omega_c} \frac{B_\zeta}{B} \frac{\partial B}{\partial Z}, \quad (28)$$

$$\begin{aligned} v^\zeta &= v_\parallel \frac{B_\zeta}{B} \frac{1}{R} + \frac{c}{B J} \left[\frac{B_Z}{B} \frac{\partial \phi}{\partial R} - \frac{B_R}{B} \frac{\partial \phi}{\partial Z} \right] \\ &+ \frac{v_\parallel^2}{\omega_c} \frac{1}{J} \left[\frac{\partial}{\partial Z} \left(\frac{B_R}{B} \right) - \frac{\partial}{\partial R} \left(\frac{B_Z}{B} \right) \right] \\ &- \frac{\mu}{m \omega_c J} \left[\frac{B_R}{B} \frac{\partial B}{\partial Z} - \frac{B_Z}{B} \frac{\partial B}{\partial R} \right], \end{aligned} \quad (29)$$

$$v^Z = v_\parallel \frac{B_Z}{B} - \frac{c}{B} \frac{B_\zeta}{B} \frac{\partial \phi}{\partial R} + \frac{v_\parallel^2}{\omega_c} \frac{1}{J} \frac{\partial}{\partial R} \left(\frac{B_\zeta}{B} \right) - \frac{\mu}{m \omega_c} \frac{B_\zeta}{B} \frac{\partial B}{\partial R}, \quad (30)$$

$$\begin{aligned} \dot{v}_\parallel &= -\frac{\mu}{m} \left(\frac{B_R}{B} \frac{\partial B}{\partial R} + \frac{B_Z}{B} \frac{\partial B}{\partial Z} \right) \\ &- \frac{q_c}{m} \left(\frac{B_R}{B} \frac{\partial \phi}{\partial R} + \frac{B_Z}{B} \frac{\partial \phi}{\partial Z} \right) \\ &- \frac{\mu v_\parallel}{m \omega_c} \frac{1}{J} \left[\frac{\partial}{\partial R} \left(\frac{B_\zeta}{B} \right) \frac{\partial B}{\partial Z} - R \frac{\partial}{\partial Z} \left(\frac{B_\zeta}{B} \right) \frac{\partial B}{\partial R} \right] \\ &- \frac{v_\parallel q_c}{m \omega_c} \frac{1}{J} \left[\frac{\partial}{\partial R} \left(\frac{B_\zeta}{B} \right) \frac{\partial \phi}{\partial Z} - R \frac{\partial}{\partial Z} \left(\frac{B_\zeta}{B} \right) \frac{\partial \phi}{\partial R} \right] \end{aligned} \quad (31)$$

For guiding center particle dynamics GTC normally uses second order Runge Kutta (RK) method (cf. Fig.4).^{34,35}

To test our integration schemes (FK and GC), we consider the linear motion of trapped particle in the core, and cross-separatrix regions using the initial conditions in Table I and Table II for DIII-D geometry, respectively. Table III and Table IV represent the initial condition for FRC geometry. The projection of the FK and GC trapped particle orbit on R-Z plane in the core and cross-separatrix regions are shown in Fig.7 for DIII-D. For both FK and GC integrators, we consider $\omega_c \Delta t = 0.292$. Both integrators correctly capture the trapped particle orbit and agree well with each other. The conservation properties of our integrators are tested with two exact constant of motion, viz., kinetic energy E and toroidal angular momentum p_ζ . Fig.8 show the relative variation of E and p_ζ for FK Boris integrator over a time period 15000 for different time step sizes in core and cross-separatrix regions.

In numerical simulation the dynamical quantities accumulate error with time. In our integrators the magnitude of the velocity provides better accuracy than the

individual components of velocity. As a result the energy conservation is better than the toroidal angular momentum. The toroidal angular momentum is conserved due to the symmetry of the magnetic field along the toroidal direction. Boris algorithm maintains adequate accuracy with 20 time steps per cyclotron period ($\omega_c \Delta t = 0.292$). Whereas the GC second order RK demonstrate that E and p_z can converge with 240 time steps per bounce period ($\omega_b \Delta t = 0.027$) in core and cross-separatrix regions. From these convergence studies, it is found that the FK Boris integrator provides better energy convergence than the second order Runge Kutta GC integrator. If there are high frequency electromagnetic perturbations, $\omega_{per} \Delta t < 1$, will set an upper bound for the time step size.

IV. FIELD ALIGNED MESH

V. DISCUSSIONS

Self-consistent simulation will be reported in future work. Also, presently we don't have the capability of handling the plasma particle loss to the material wall, recycling the neutral particles, and calculating the Monte-Carlo neutral particle transport with a charge exchange and ionization interaction with the plasma.

ACKNOWLEDGMENTS

This work is supported by US Department of Energy (DOE) SciDAC GSEP Program, China National Magnetic Confinement Fusion Energy Research Program, Grant No. 2013GB111000 and National Science Foundation of China Grant No. 11275162. Simulations were performed using the super computer resources of the Oak Ridge Leadership Computing Facility at Oak Ridge National Laboratory (DOE Contract No. DE-AC05-00OR22725), and the National Energy Research Scientific Computing Center (DOE Contract No. DE-AC02-05CH11231).

¹A. Loarte et al., "Chapter 4: Power and particle control," Nucl. Fusion **47**, S203 (2007).

²R. Cesario, L. Amicucci, A. Cardinali, C. Castaldo, M. Marinucci, L. Panaccione, F. Santini, O. Tudisco, M. L. Apicella, G. Calabro, C. Cianfarani, D. Frigione, A. Galli, G. Mazzitelli, C. Mazzotta, V. Pericoli, G. Schettini, A. A. Tuccillo, and FTU Team, "Current drive at plasma densities required for thermonuclear reactors," Nat. Commun. **1**, 55 (2010).

³F. Wising, D.A. Knoll, S.I. Krasheninnikov, T.D. Rognlien, and D.J. Sigmar, "Simulation of detachment in ITER geometry using the UEDGE code and a fluid neutral model," Contrib. Plasma Phys., **36**, 309 (1996).

⁴V. Rozhansky, E. Kaveeva, P. Molchanov, I. Veselova, S. Voskoboinikov, D. Coster, G. Counsell, A. Kirk, S. Lisgo, "New B2SOLPS5.2 transport code for H-mode regimes in tokamaks," Nucl. Fusion **49**, 025007 (2007).

⁵S. I. Braginskii, Reviews of Plasma Physics, New York: Consultants Bureau, **1**, 205 (1965).

⁶A. Chankin, D. Coster, N. Asakura, X. Bonnin, G. Conway, G. Corrigan, S. Erents, W. Fundamenski, J. Horacek, A. Kallenbach, M. Kaufmann, C. Konz, K. Lackner, H. Miller, J. Neuhauser, R. Pitts, M. Wischmeier, "Discrepancy between modelled and measured radial electric fields in the scrape-off layer of divertor tokamaks: a challenge for 2D fluid codes?" Nucl. Fusion **47**, 479 (2007).

⁷S. K. Erents, R.a. Pitts, W. Fundamenski, J.P. Gunn, G.F. Matthews, "A comparison of experimental measurements and code results to determine flows in the JET SOL," Plasma Phys. Control. Fusion **46**, 1757 (2004).

⁸M. Wischmeier, M. Groth, S. Wiesen, S. Potzel, L. Aho-Mantila, D. P. Coster, R. Dux, C. Fuchs, a. Kallenbach, H.W. Miller, D. Reiter, a. Scarabosio, Assessment of edge modeling in support of ITER, J. Nucl. Mater. **415**, S523, (2011).

⁹W. Stacey, "Effect of ion orbit loss on distribution of particle, energy and momentum sources into the tokamak scrape-off layer," Nucl. Fusion **53**, 063011 (2013).

¹⁰C. S. Chang, S. Kue, H. Weitzner, "X-transport: a baseline non-ambipolar transport in a diverted tokamak plasma edge," Phys. Plasmas **9**, 3884 (2002).

¹¹J. T. Omotani, B.D. Dudson, "Non-local approach to kinetic effects on parallel transport in fluid models of the scrape-off layer," Plasma Phys. Control. Fusion **55**, 055009 (2013).

¹²J. A. Wesson, Effect of temperature gradient on plasma sheath, Plasma Phys. Control. Fusion **37**, 1459 (1995).

¹³A. Kuley and V. K. Tripathi, "Stabilization of ion temperature gradient driven modes by lower hybrid wave in a tokamak," Physics of Plasmas **16**, 032504 (2009).

¹⁴A. Kuley and V. K. Tripathi, "Parametric upconversion of lower hybrid wave by runaway electrons in tokamak," Physics of Plasmas **17**, 062507 (2010).

¹⁵A. Kuley, C. S. Liu, and V. K. Tripathi, "Lower hybrid destabilization of trapped electron modes in tokamak and its consequences for anomalous diffusion," Physics of Plasmas **17**, 072506 (2010).

¹⁶Z. Lin, T. S. Hahm, W. W. Lee, W. M. Tang and R. B. White, "Turbulent Transport Reduction by Zonal Flows: Massively Parallel Simulations," Science **281**, 1835 (1998).

¹⁷Z. Lin, W. M. Tang and W. W. Lee, "Large orbit neoclassical transport," Phys. Rev. Lett. **78**, 456 (1997).

¹⁸G. Dong and Z. Lin, "Effects of Magnetic Islands on Bootstrap Current in Toroidal Plasmas," Nuclear Fusion **57**, 036009 (2017).

¹⁹X. Liao, Z. Lin, I. Holod, Y. Xiao, B. Li and P. B. Snyder, "Microturbulence in DIII-D tokamak pedestal. III. Effects of collisions," Phys. Plasmas **23**, 122507 (2016).

²⁰X. Liao, Z. Lin, I. Holod, Y. Xiao, B. Li and G.Y. Sun, "Microturbulence in DIII-D tokamak pedestal. IV. Electrostatic turbulent transport," Phys. Plasmas **23**, 122305 (2016).

²¹D. P. Fulton, C. K. Lau, L. Schmitz, I. Holod, Z. Lin, T. Tajima, M. W. Binderbauer and TAE Team, "Gyrokinetic simulation of driftwave instability in field-reversed configuration," Phys. Plasmas **23**, 056111 (2016).

²²I. Holod, D. Fulton, Z. Lin, "Microturbulence in DIII-D tokamak pedestal. II. Electromagnetic instabilities," Nuclear Fusion **55**, 093020 (2015).

²³I. Holod, Z. Lin, S. Taimourzadeh, R. Nazikian, D. Spong, and A. Wingen, "Effects of Resonant Magnetic Perturbations on Microturbulence in DIII-D Pedestal," Nuclear Fusion **57**, 016005 (2017).

²⁴Y. Xiao, I. Holod, Z. X. Wang, Z. Lin, and T. Zhang, "Gyrokinetic particle simulation of microturbulence for general magnetic geometry and experimental profiles," Phys. Plasmas **22**, 022516 (2015).

²⁵H. S. Zhang, Z. Lin, and I. Holod, "Nonlinear Frequency Oscillation of Alfvén Eigenmodes in Fusion Plasmas," Phys. Rev. Lett. **109**, 025001 (2012).

²⁶W. Deng, Z. Lin, I. Holod, Z. Wang, Y. Xiao, and H. Zhang, "Linear properties of reversed shear Alfvén eigenmodes in DIII-D tokamak," Nuclear Fusion **52**, 043006 (2012).

- ²⁷D. A. Spong, E. M. Bass, W. Deng, W. W. Heidbrink, Z. Lin, B. Tobias, M. A. Van Zeeland, M. E. Austin, C. W. Domier, N. C. Luhmann, Jr., "Verification and validation of linear gyrokinetic simulation of Alfvén eigenmodes in the DIII-D tokamak," *Phys. Plasmas* **19**, 082511 (2012).
- ²⁸Zhixuan Wang, Zhihong Lin, Ihor Holod, W. W. Heidbrink, Benjamin Tobias, Michael Van Zeeland, and M. E. Austin, "Radial Localization of Toroidicity-Induced Alfvén Eigenmodes," *Phys. Rev. Lett.* **111**, 145003 (2013).
- ²⁹J. McClenaghan, Z. Lin, I. Holod, W. Deng, and Z. Wang, "Verification of gyrokinetic particle simulation of current-driven instability in fusion plasmas. I. Internal kink mode," *Phys. Plasmas* **21**, 122519 (2014).
- ³⁰Dongjian Liu, Wenlu Zhang, Joseph McClenaghan, Jiaqi Wang, Zhihong Lin, "Verification of Gyrokinetic Particle Simulation of Current-driven Instability in Fusion Plasmas. II. Resistive Tearing Mode," *Phys. Plasmas* **21**, 122520 (2014).
- ³¹Dongjian Liu, Jian Bao, Tao Han, Jiaqi Wang, Zhihong Lin, "Verification of Gyrokinetic Particle Simulation of Current-driven Instability in Fusion Plasmas. III. Collisionless Tearing Mode," *Phys. Plasmas* **23**, 022502 (2016).
- ³²A. Kuley, Z. X. Wang, Z. Lin, and F. Wessel, "Verification of particle simulation of radio frequency waves in fusion plasmas," *Physics of Plasmas* **20**, 102515 (2013).
- ³³J. Bao, Z. Lin, A. Kuley, and Z. X. Lu, "Particle simulation of lower hybrid wave propagation in fusion plasmas," *Plasma Phys. Contr. Fusion* **56**, 095020 (2014).
- ³⁴A. Kuley, Z. Lin, J. Bao, X. S. Wei, Y. Xiao, W. Zhang, G. Y. Sun, N. J. Fisch, "Verification of nonlinear particle simulation of radio frequency waves in tokamak," *Physics of Plasmas* **22**, 102515 (2015).
- ³⁵A. Kuley, Z. Lin, J. Bao, X. S. Wei, Y. Xiao, "Nonlinear Particle Simulation of Ion Cyclotron Waves in Toroidal Geometry," *AIP Conference Proceedings* **1689**, 060008 (2015).
- ³⁶J. Bao, Z. Lin, A. Kuley, "Global particle simulation of lower hybrid wave propagation and mode conversion in tokamaks," *AIP Conference Proceedings* **1689**, 080008 (2015).
- ³⁷J. Bao, Z. Lin, A. Kuley, and Z. X. Wang, "Electromagnetic particle simulation of toroidal effects on linear mode conversion and absorption of lower hybrid waves," *Nucl. Fusion* **56**, 066007 (2016).
- ³⁸J. Bao, Z. Lin, A. Kuley, and Z. X. Wang, "Nonlinear electromagnetic formulation for particle simulation of lower hybrid waves in toroidal geometry," *Phys. Plasmas* **23**, 062501 (2016).
- ³⁹D. P. Fulton, C. K. Lau, I. Holod, Z. Lin, and S. Dettrick, "Gyrokinetic Particle Simulation of a Field Reversed Configuration," *Phys. Plasmas* **23**, 012509 (2016).
- ⁴⁰C. K. Lau, D. P. Fulton, I. Holod, Z. Lin, M. Binderbauer, T. Tajima, and L. Schmitz, "Drift-wave Stabilities in the Field-Reversed Configuration," submitted to *Nucl. Fusion*, 2017.
- ⁴¹L.L. Lao, J.R. Ferron, R.J. Groebner, W. Howl, H. St. John, E.J. Strait and T.S. Taylor, "Equilibrium analysis of current profiles in tokamaks," *Nucl. Fusion* **30**, 1035 (1990).
- ⁴²Q. Ren, M. S. Chu, L. L. Lao, and R. Srinivasan, "High spatial resolution equilibrium reconstruction," *Plasma Phys. Controlled Fusion* **53**, 095009 (2011).
- ⁴³L. Galeotti, D. C. Barnes, F. Ceccherini and F. Pegoraro, "Plasma equilibria with multiple ion species: Equations and algorithm," *Phys. Plasmas* **18**, 082509 (2011).
- ⁴⁴Kyuhoo Kim, C.S. Chang, Janghoon Seo, S. Ku and W. Choe, "What happens to full-f gyrokinetic transport and turbulence in a toroidal wedge simulation?," *Phys. Plasmas* **24**, 012306 (2017).
- ⁴⁵F. Hariri, M. Ottaviani, "A flux-coordinate independent field-aligned approach to plasma turbulence simulations," *Computer Physics Communications* **184**, 2419 (2013).
- ⁴⁶X. S. Wei, Y. Xiao, A. Kuley, and Z. Lin, "Method to integrate full particle orbit in toroidal plasmas," *Physics of Plasmas* **22**, 092502 (2015).
- ⁴⁷J. Boris, in *Proceedings of the fourth international conference on numerical simulation of plasmas* (NRL, 1970) pp. 367.
- ⁴⁸C. K. Birdsall and A. B. Langdon, *Plasma physics via computer simulation* (Institute of Physics, New York, 2005).
- ⁴⁹A. J. Brizard and T. S. Hahm, "Foundations of nonlinear gyrokinetic theory," *Rev. Mod. Phys.* **79**, 421 (2007).
- ⁵⁰B. J. Sturdevant, Y. Chen, Z. Lin, and S. E. Parker, "Simulation of the Toroidal Ion Temperature Gradient Instability with Fully Kinetic Ions," *Phys. Plasmas*, (submitted).